Supporting Information

Photoelectrochemical reduction of CO_2 catalyzed by 3D core-shell $NiMoO_4$@ZnO heterojunction with bicentre at (111) plane and assistance of thermal electrons

Youzhi Cao,[a] Yan Wei,[a] Wenrui Wan,[a] Chunyan Liu,[a] Changwan Zhuang,[a] Can Gong,[a] Linhong Nan,[a] Qiaolan Zhang,*[a] Hong Gao,*[a] Jiazang Chen[b] and Huanwang Jing*[ab]

[a.] *State Key Laboratory of Applied Organic Chemistry, College of Chemistry and Chemical Engineering, Lanzhou University, 222 South Tianshui Road, Lanzhou, 730000, PR China. E-mail: hwjing@lzu.edu.cn*
[b.] *State Key Laboratory of Coal Conversion, Institute of Coal Chemistry, Chinese Academy of Sciences, Taiyuan, 030001, PR China*

Experimental section

Prepared $BiVO_4$ photoanode

Nanoporous $BiVO_4$ photoanode were prepared according to the previous reports.[1] In detail, the 20 mL solutions for electrodeposition were prepared by 0.39 g $Bi(NO_3)_3$ and 1.33 g KI, which was then adjusted to pH=1.7 with a few drops of concentrated HNO_3. This solution was uniformed mixing with 8 mL of ethanol containing 0.2 g *p*-benzoquinone. A standard three-electrode cell equipped with a FTO working electrode, an Ag/AgCl reference, and a platinum counter electrode was used for electrodeposition. Deposition was carried out potentiostatically at -0.1 V *vs.* Ag/AgCl for 5 min and gave rise to the precipitation of crystalline BiOI on the FTO. 0.15-0.2 mL of a dimethyl sulfoxide (DMSO) solution containing 0.2 M vanadyl acetylacetonate ($VO(acac)_2$) was placed on the BiOI electrode (1.0×2.5 cm)and heated in a muffle furnace at 450 °C for 2 h in air to convert BiOI to $BiVO_4$ (ramping rate = 5 °C·min^{-1}). Excess V_2O_5 present in the $BiVO_4$ electrodes was removed by soaking them in 1 M NaOH solution with gentle stirring until getting a clean surface. Finally, the resulting pure orange $BiVO_4$ photoanode were rinsed with DI water and dried at room temperature.

$^{13}CO_2$ isotopic labeling experiment

The isotopic labelling experiment using $^{13}CO_2$ for CO_2 reduction was carried out in the cell using the new photocathode $NiMoO_4$/ZnO-3. After bubbling argon for 30 min to eliminate

oxygen from the entire system, $^{13}CO_2$ gas was introduced into the system for 30 min. The related artificial photosynthesis was performed for 2 h under simulated light irradiation at -0.8 V *vs.* SCE.

Electrode Surface Temperature Measurement.

The temperature of the electrode surface was measured by an infrared thermal camera (FLIR A615). The electrodes were prepared using the same procedure as we described in previous methods. The as-prepared electrode was placed under the light source in the dark state (PLS-SXE300C, 100 $mW \cdot cm^{-2}$). The temperature distribution on the electrode's surface was collected under an applied constant light density.

Operando FT-IR spectroscopy measurements

The operando Fourier transform infrared (FT-IR) spectra was conducted on a TENSOR27 spectrometer (Bruker) equipped with a DigiTectTM detector cooled by liquid nitrogen and IN350-T fiber probe (Bruker). The measurements were carried out in 0.1 M Na_2SO_3 H_2O electrolyte and 0.1 M Na_2SO_3 D_2O at room temperature. A constant flow of CO_2 gas was purged into the electrolyte for 1 h to reach saturation and maintain it throughout the photoelectrochemical experiments. All spectroscopic measurements were conducted at a 4 cm^{-1} spectral resolution and 32 scans. The spectra were presented in absorbance, with positive and negative peaks showing an increase and decrease in signal, respectively.

Theoretical calculations

All the simulations in this work were performed according to DFT within the framework of the all-electron projector augmented wave (PAW) method, as implemented in the VASP code. We adopted the Perdew-Burke-Ernzerhof (PBE) functional using the generalized gradient approximation (GGA) level of theory for the valence electron-ion interaction, a plane-wave kinetic energy cutoff of 400 eV. The self-consistent-field (SCF) calculations are finished until both the total energy difference between two iterations and the Hellman Feynman forces on atoms are converged to within 1×10^{-5} eV and less than 0.05 eV $Å^{-1}$, respectively. The k-point sampling uses the Monkhorst–Pack scheme with a 3×3×1 mesh. The (111) plane of the monoclinic $NiMoO_4$ (space group number of 12) was experimentally confirmed to be very stable crystal planes, which are representatively chosen for our calculations. The surfaces are simulated as slabs, where a vacuum layer of 15 Å is chosen in the z direction to avoid interactions between periodically repeated slabs.

Quantify of liquid products.

$$\text{Rate}_{\text{liquid product}} = \frac{C_{DMSO}(\mu M) \times \text{Area}_{product}/\text{Area}_{DMSO}}{\text{Time(h)} \times 1(cm^2)} \quad (1)$$

C2 Selectivity have been calculated according to the following equations:

$$\text{C2 Selectivity}(\%) = \frac{\sum (\text{moles of C2 products} \times n)}{\sum (\text{moles of products} \times n)} \quad (2)$$

n (electron transfer number) = 2, $HCOO^-$, H_2; 8, CH_3COOH; 10, $(OH)_2CHCH_2OH$; 12, CH_3CH_2OH; 16, CH_3COCH_3.

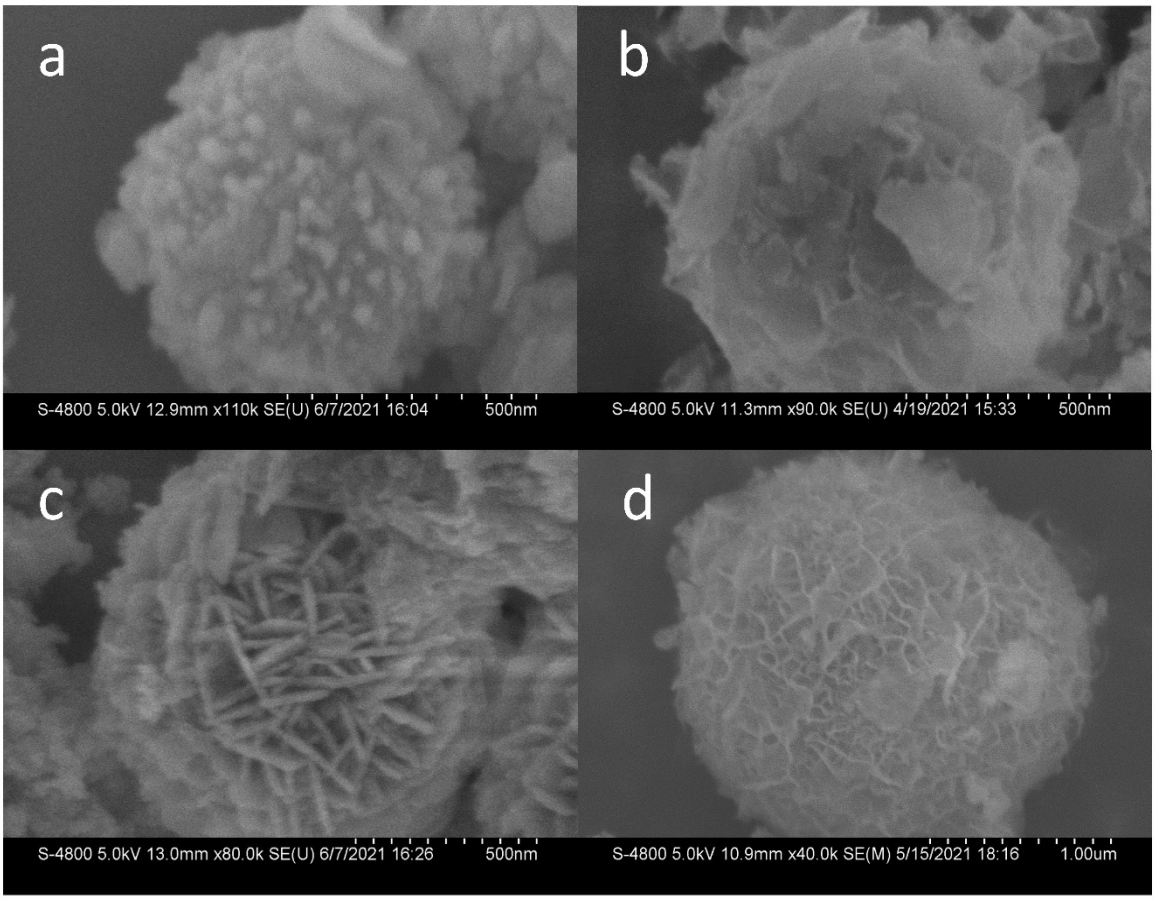

Figure S1. SEM images of (a) $NiMoO_4$/ZnO-1, (b) $NiMoO_4$/ZnO-2, (c) $NiMoO_4$/ZnO-4 and (d) $NiMoO_4$

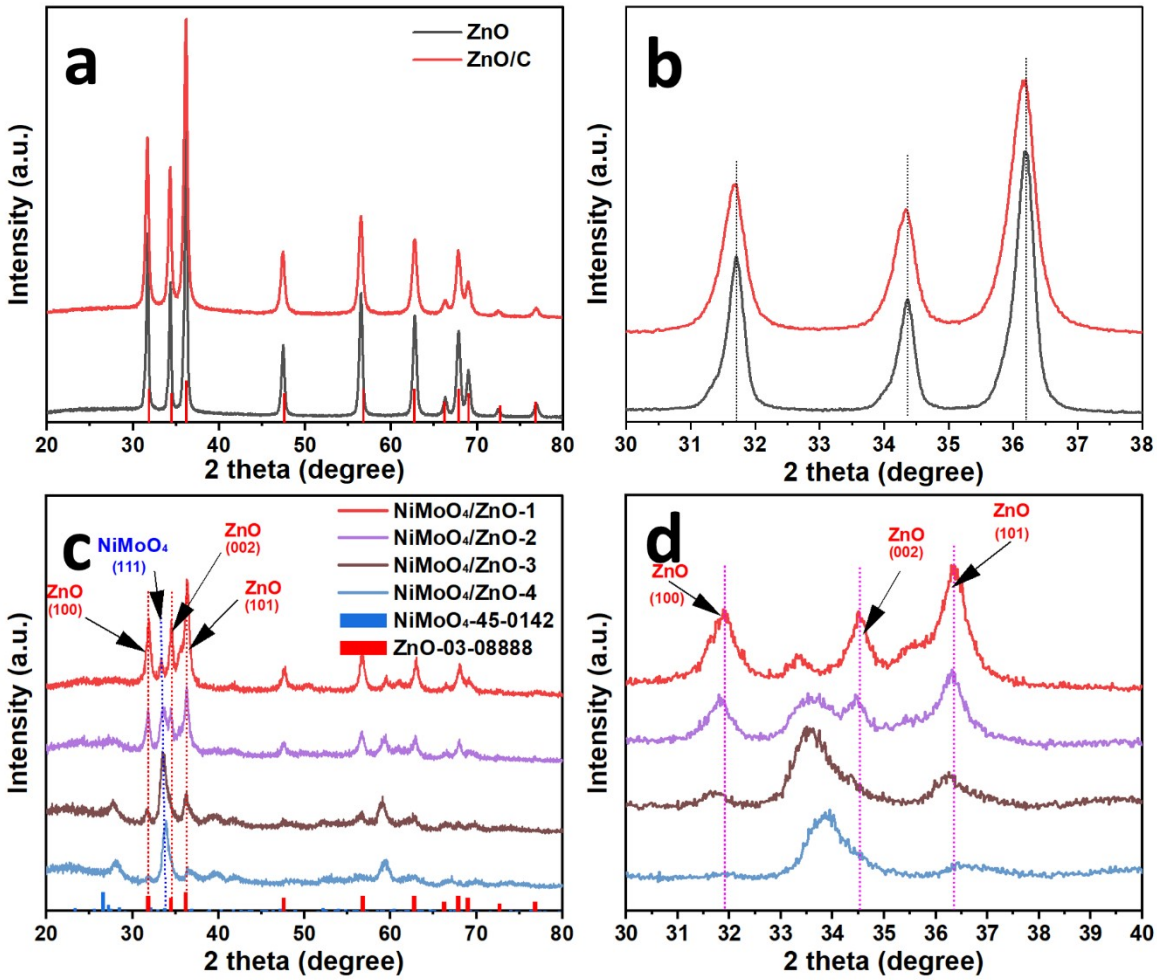

Figure S2. (a) XRD patterns of ZnO/C and (b) its partial enlarged image; (c) XRD patterns of $NiMoO_4$/ZnO heterojunction and (d) its partial enlarged image

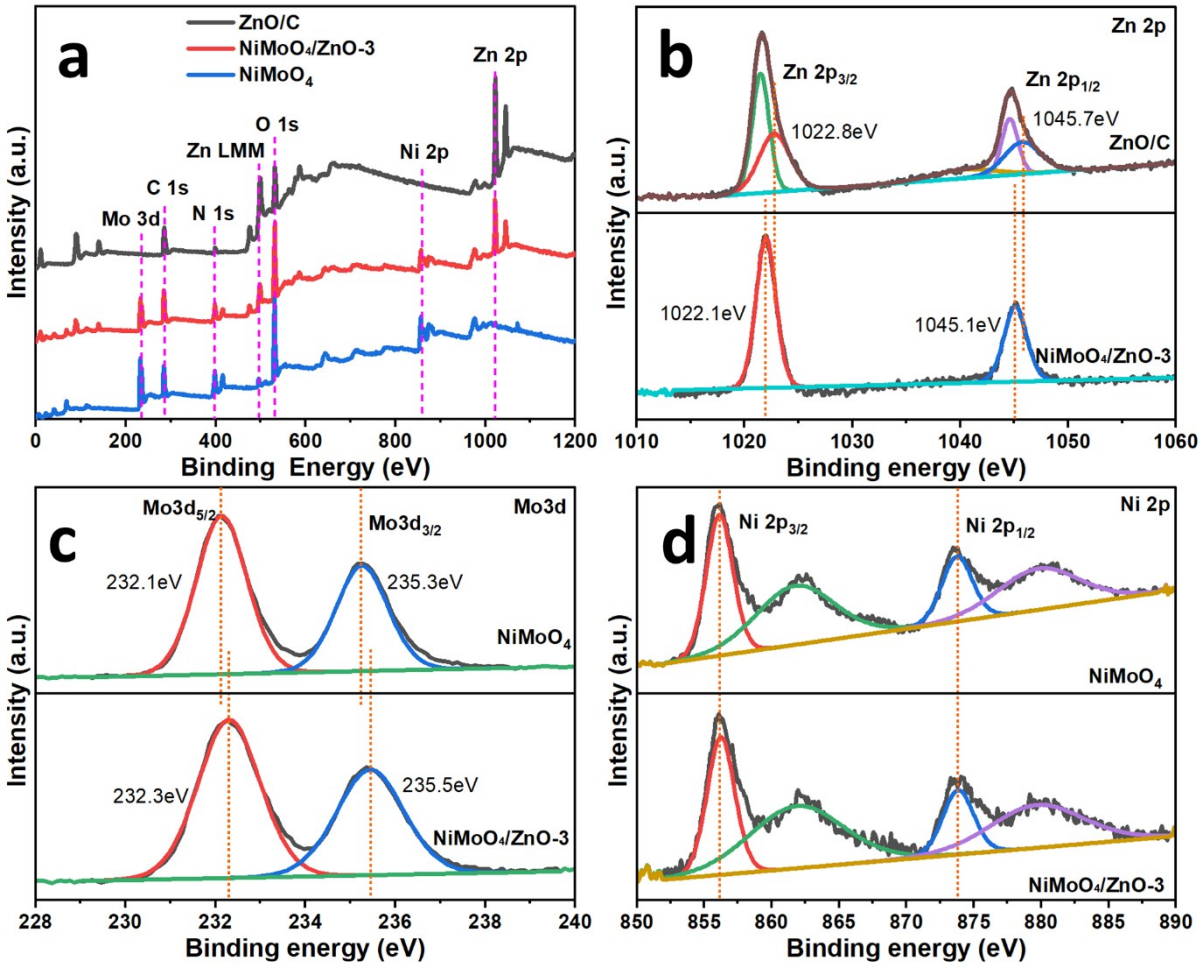

Figure S3. (a) XPS survey spectrum for ZnO/C, $NiMoO_4$/ZnO-3 and $NiMoO_4$, and high-resolution XPS spectra of (b) Zn 2p, (c) Mo 3d and (d) Ni 2p

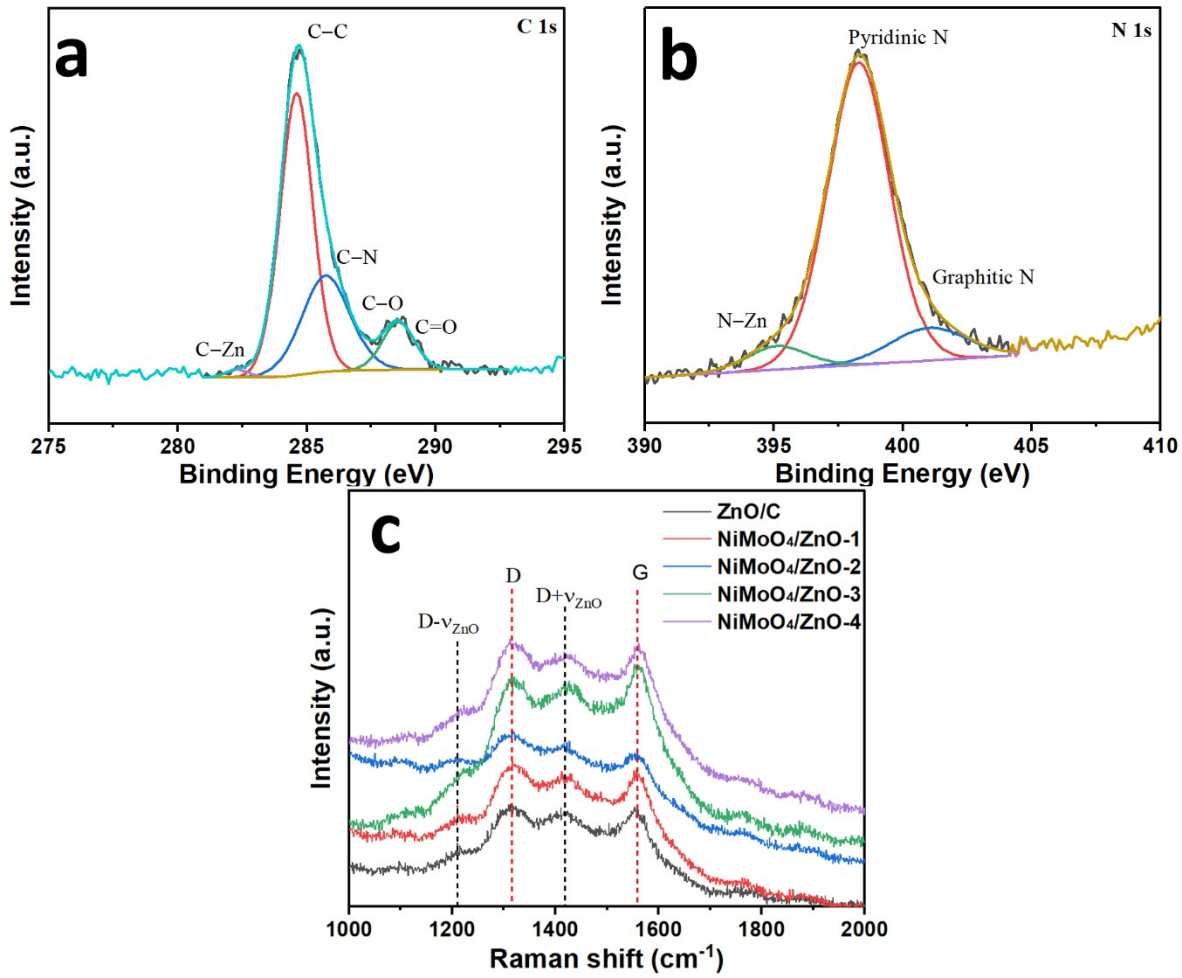

Figure S4. The high-resolution XPS spectra of (a) C 1s and (b) N 1s of ZnO/C; (c) Raman spectra of $NiMoO_4$/ZnO-x

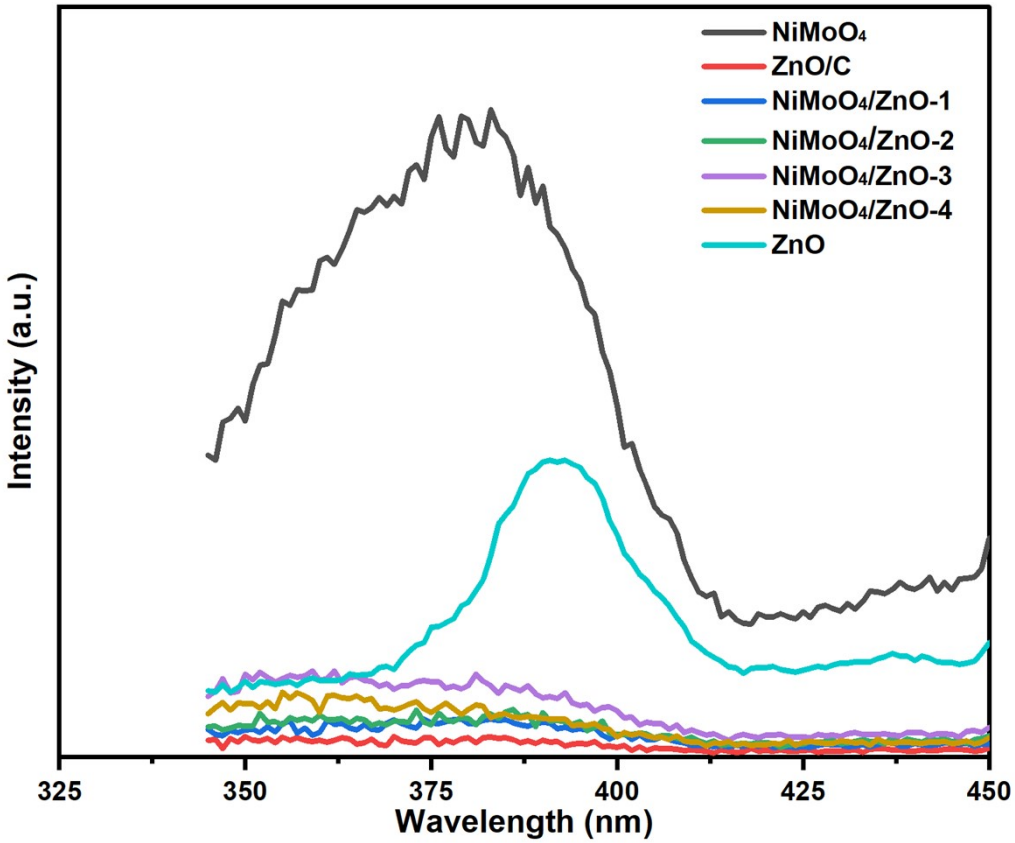

Figure S5. PL spectra of the different samples

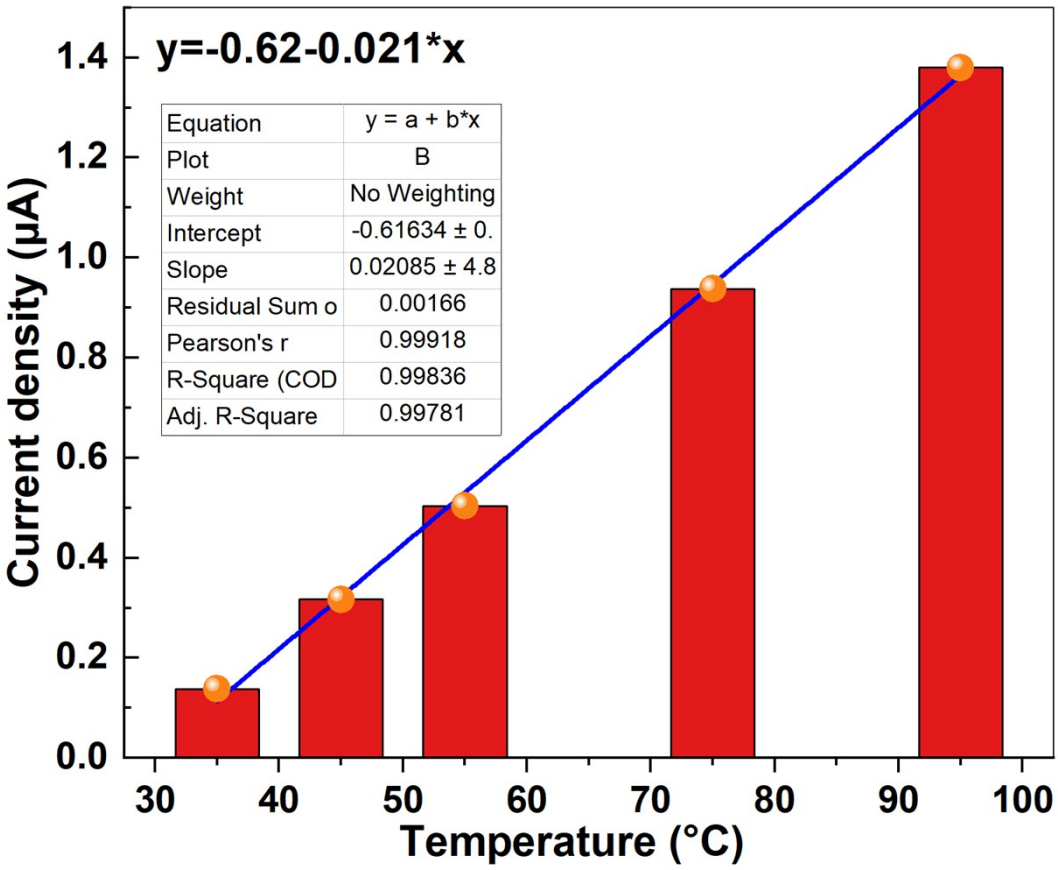

Figure S6. Thermal electron detection experiments at different temperatures

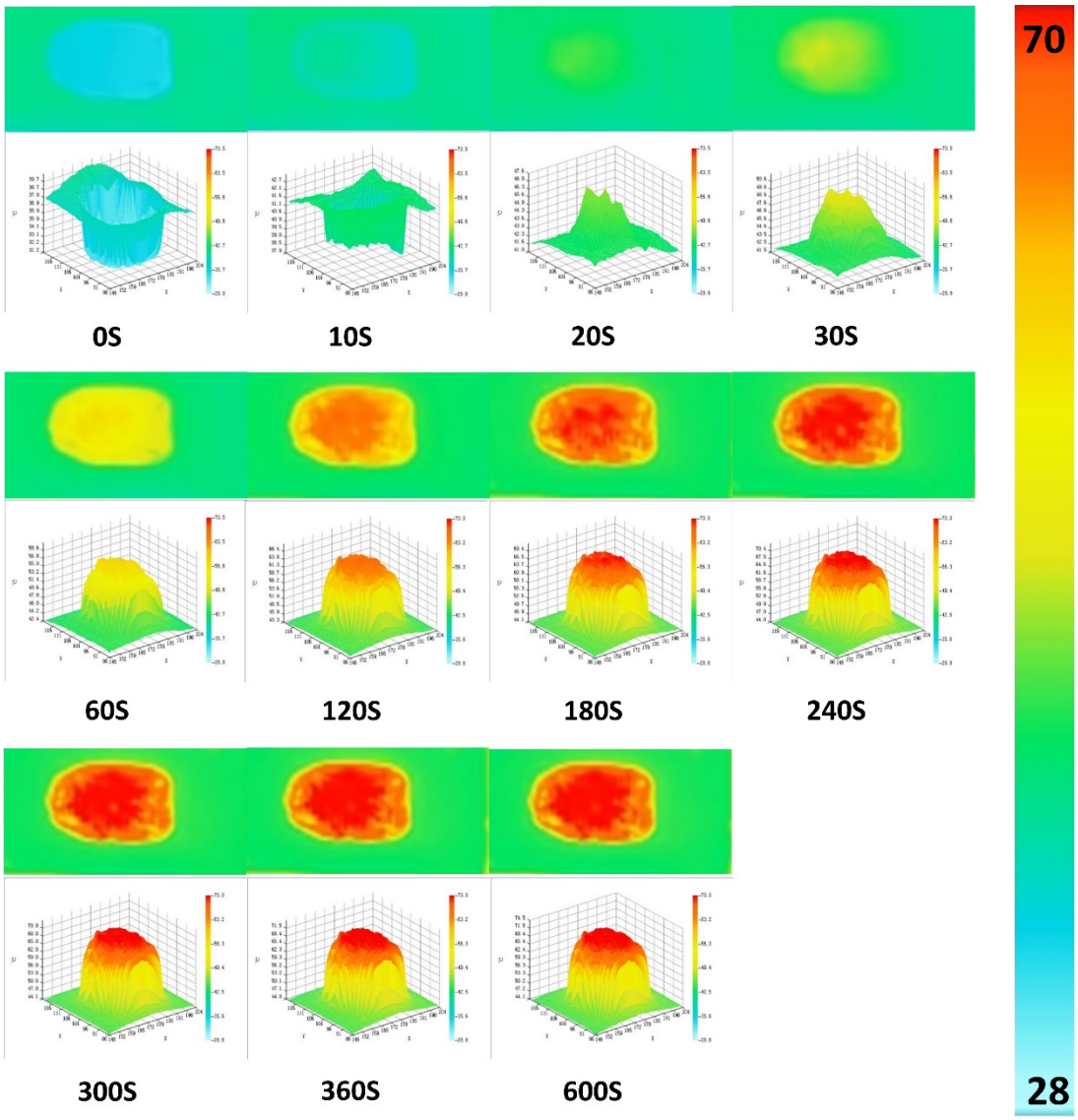

Figure S7. Infrared thermal imaging and 3D infrared thermal images of ZnO/C at different times of illumination at constant light intensity

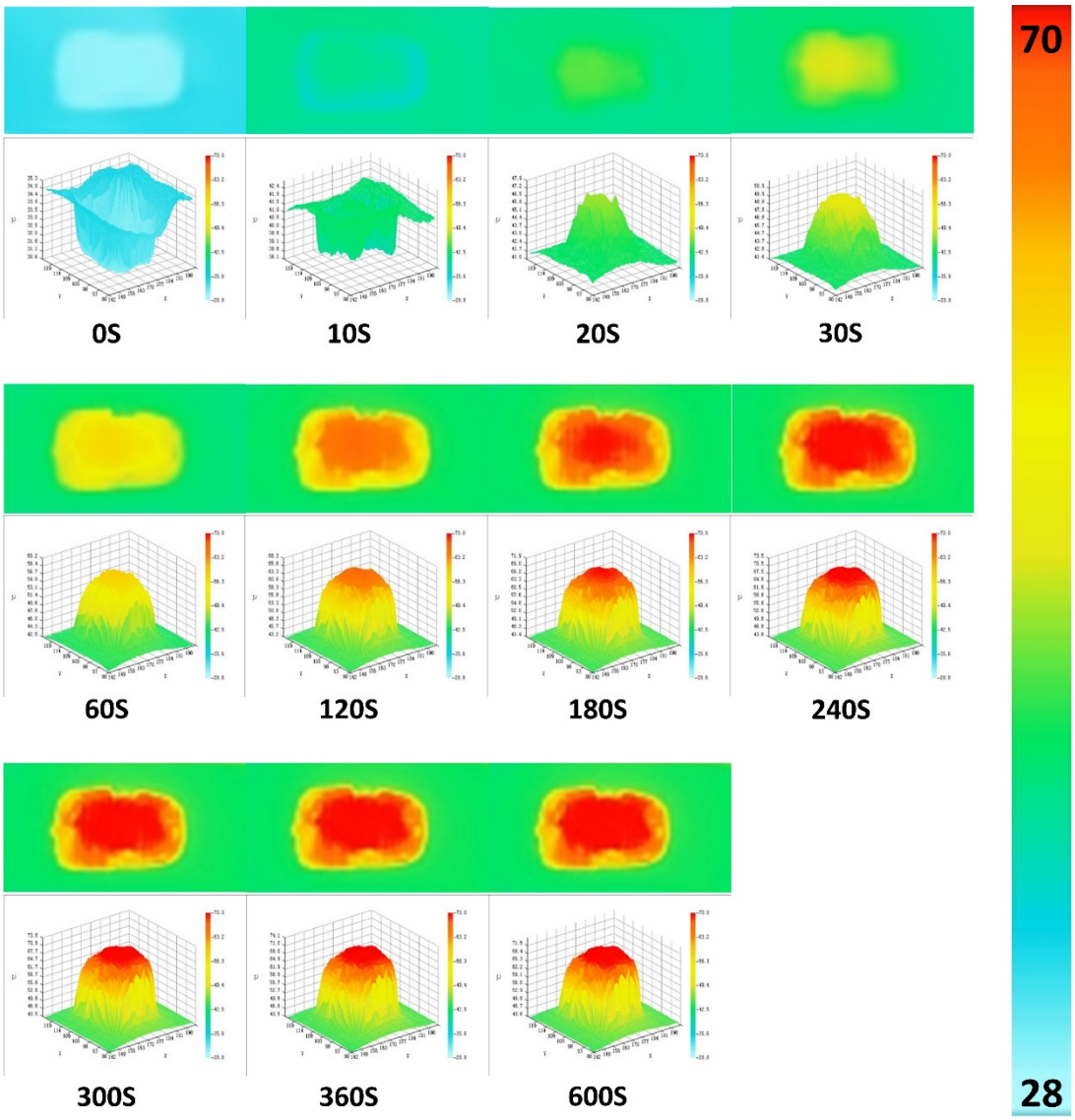

Figure S8. Infrared thermal imaging and 3D infrared thermal images of $NiMoO_4$/ZnO-3 at different times of illumination at constant light intensity

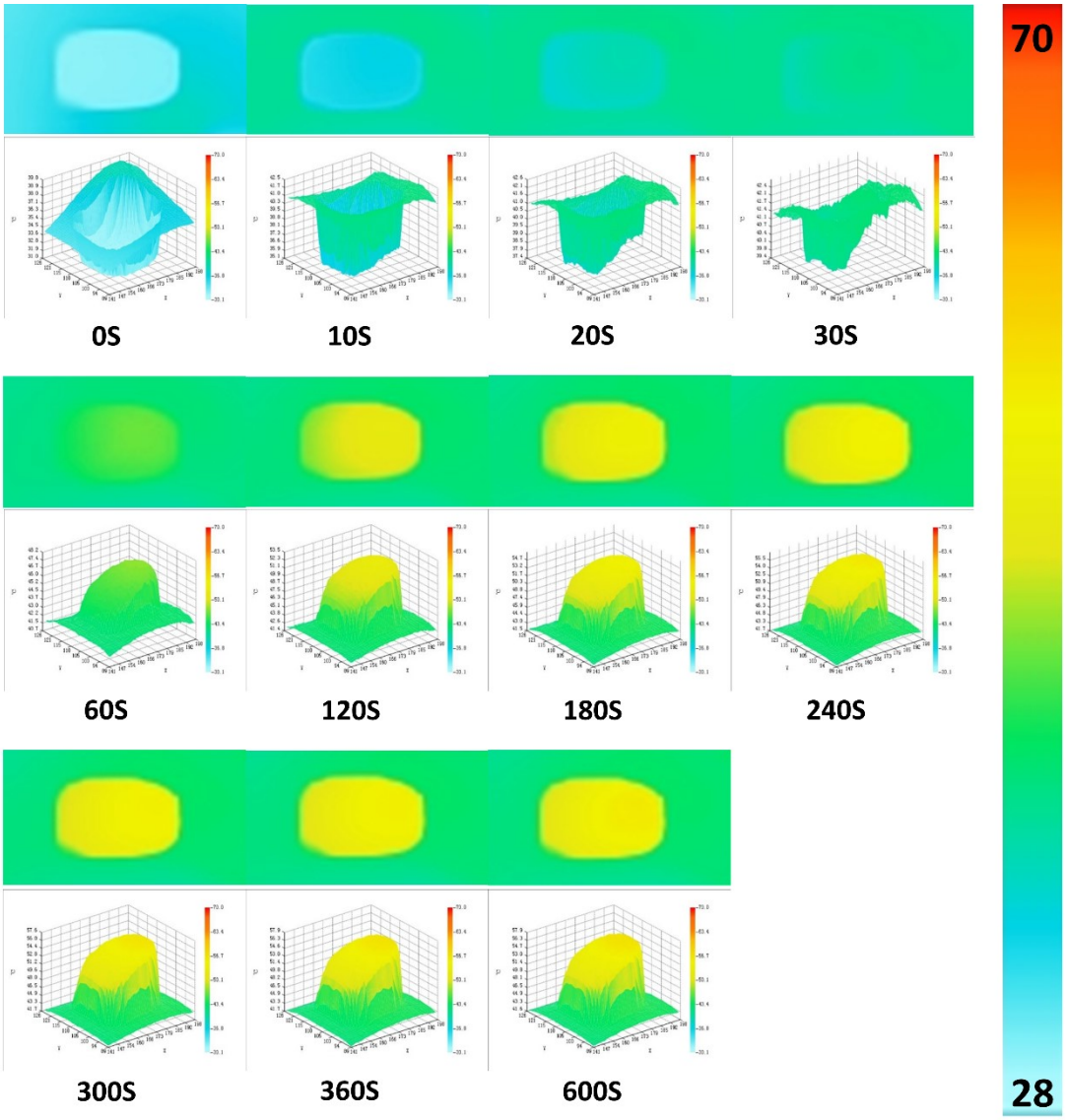

Figure S9. Infrared thermal imaging and 3D infrared thermal images of $NiMoO_4$ at different times of illumination at constant light intensity

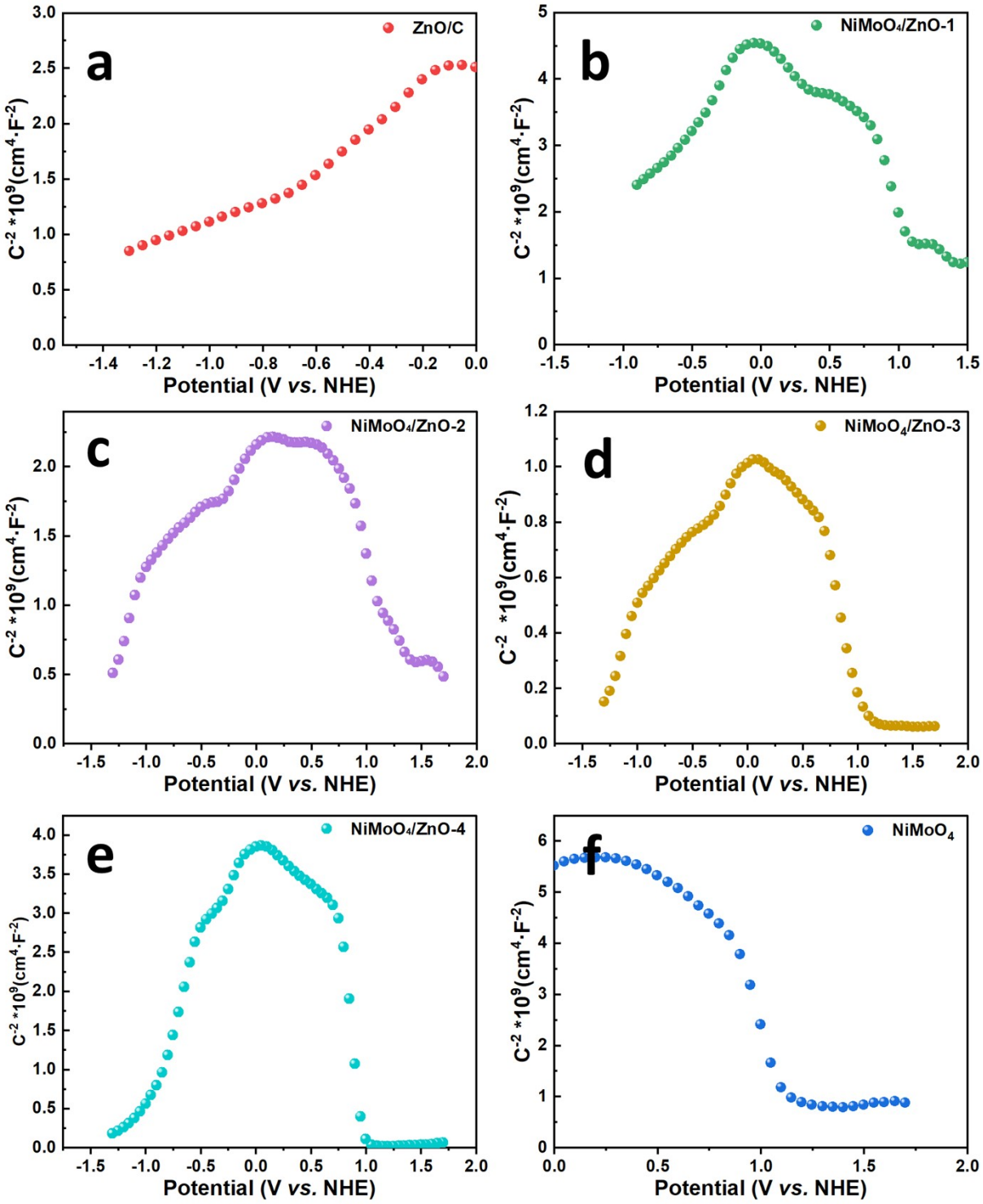

Figure S10. Mott-Schottky plots of different photocathodes

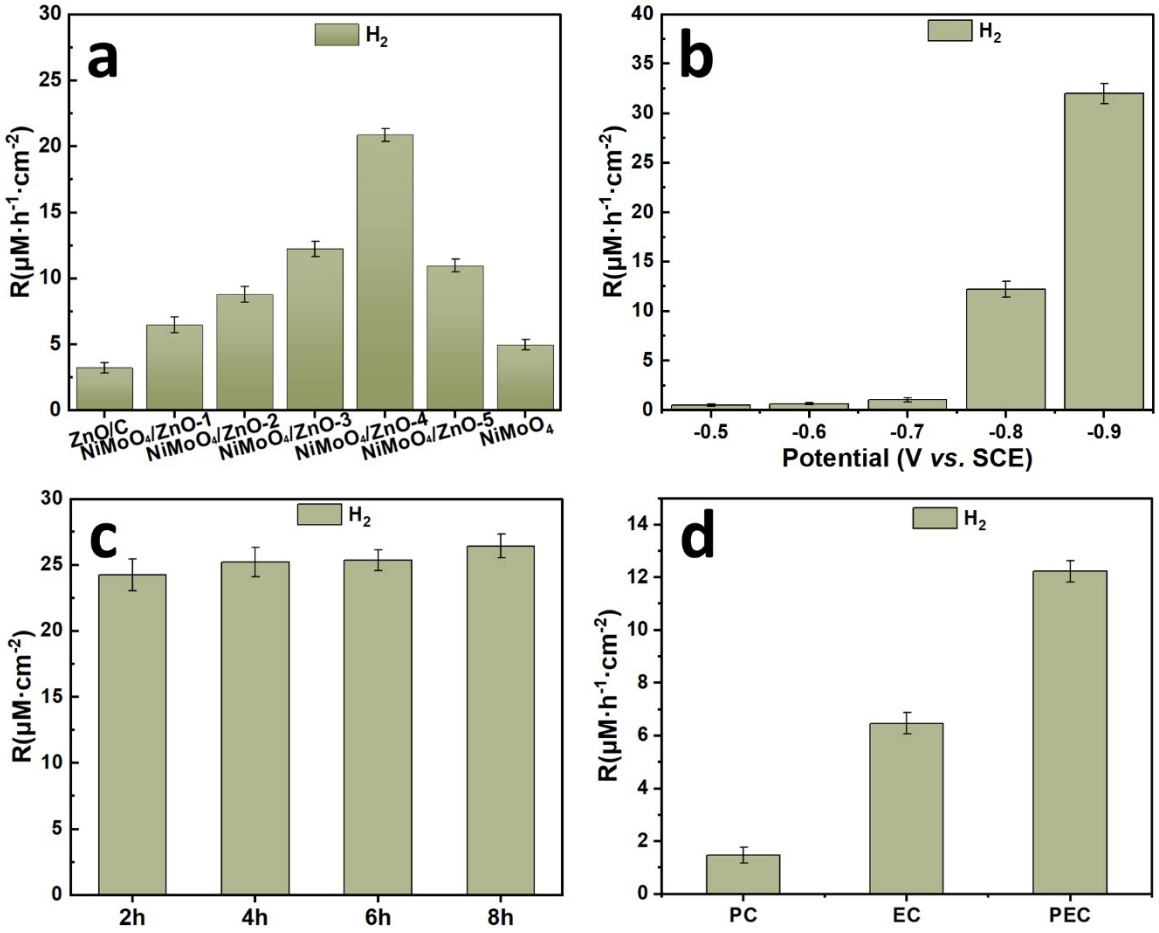

Figure S11. Results of PEC reduction of CO_2. (a) The formation rates of H_2 under –0.8 V *vs.* SCE over different photocathodes, (b) formation rates of H_2 under different voltages over $NiMoO_4$/ZnO-3, (c) during the CO_2 reduction process, H_2 accumulation experiment per 2 h over $NiMoO_4$/ZnO-3 at –0.8 V *vs.* SCE, (d) formation rates of H_2 under EC, PC and PEC condition over $NiMoO_4$/ZnO-3 at –0.8 V *vs.* SCE

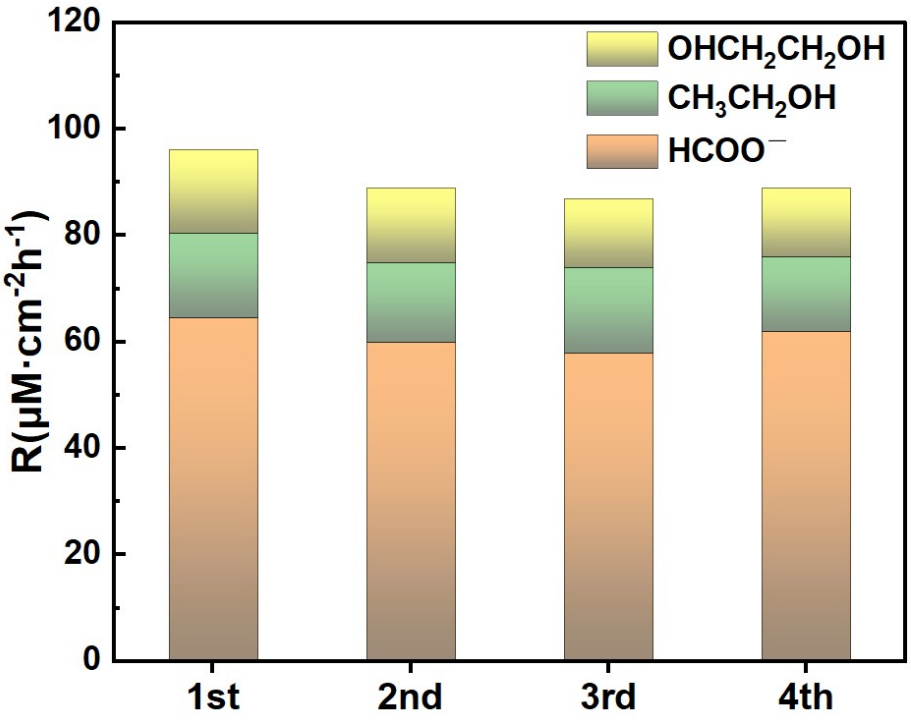

Figure S12. Stability experiment of CO_2 reduction per 2 h over $NiMoO_4$/ZnO-3 at –0.8 V *vs.* SCE

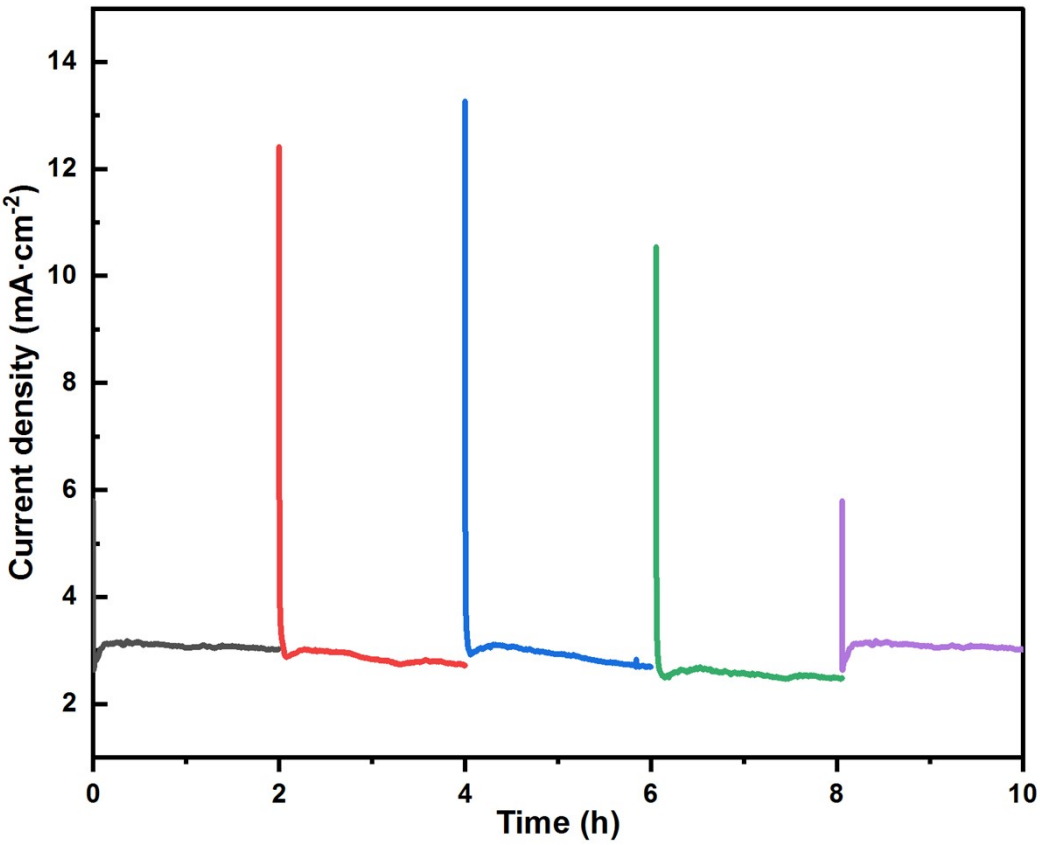

Figure S13. Stability test of PEC reduction of CO_2 using $NiMoO_4$/ZnO-3 at –0.8 V *vs.* SCE

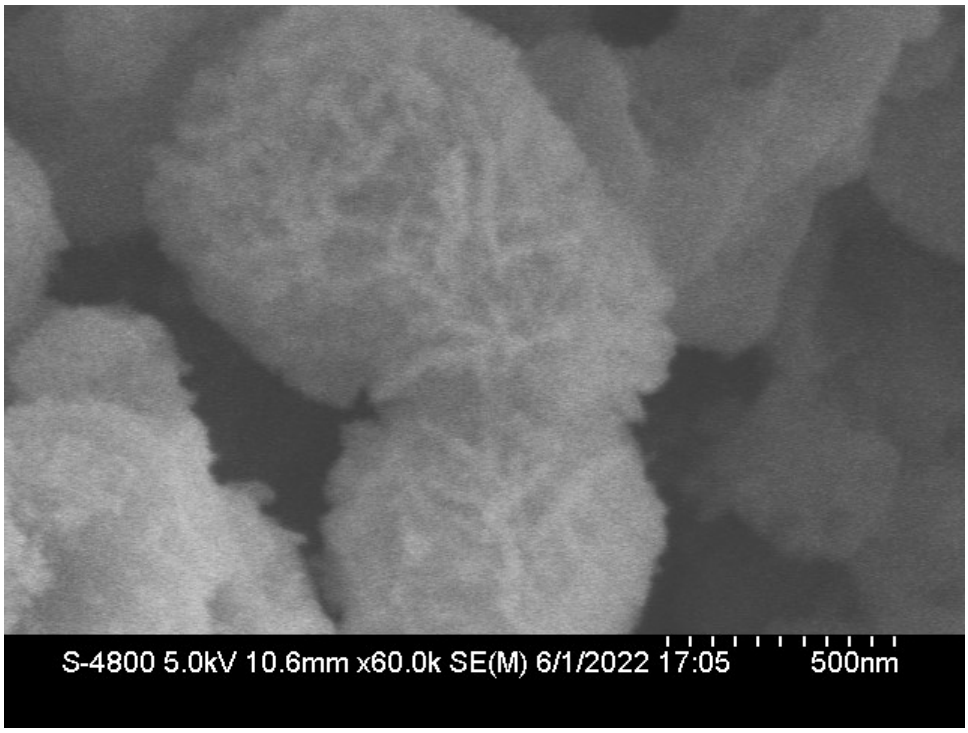

Figure S14. SEM images of $NiMoO_4$/ZnO -3 after PEC reduction of CO_2 8 h at –0.8 V *vs.* SCE

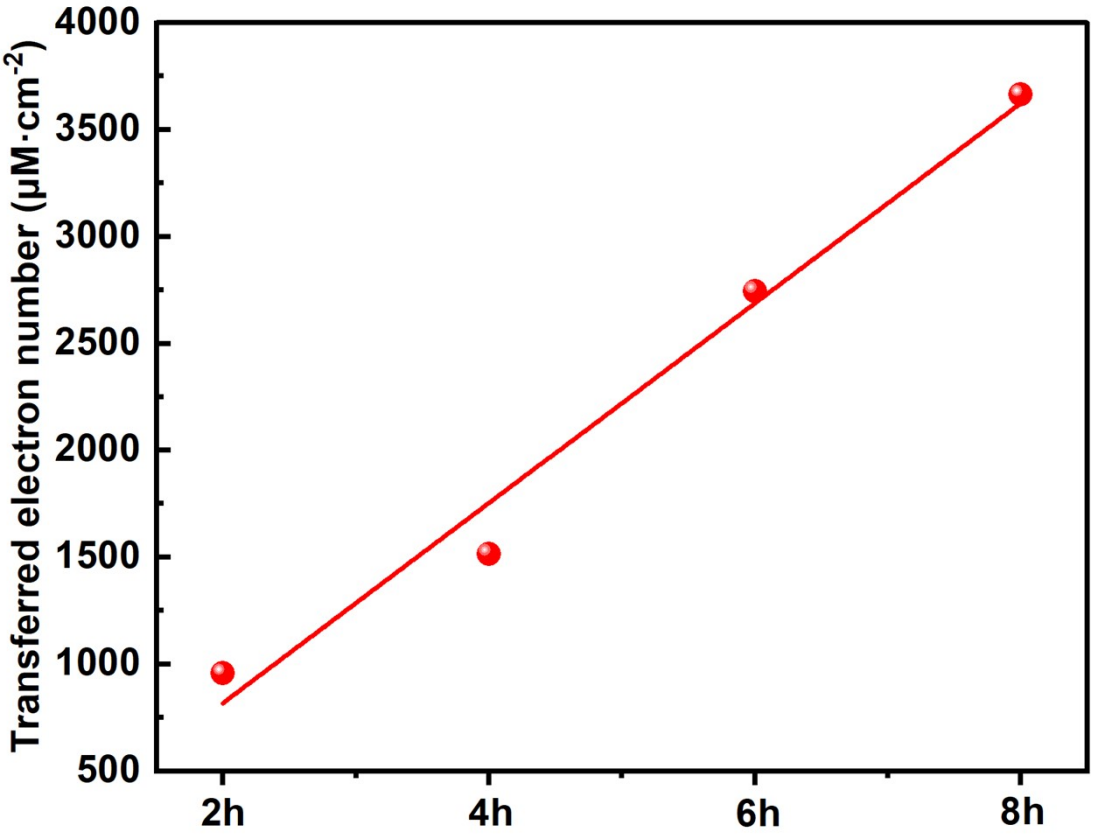

Figure S15. Transferred electron number in the CO_2 reduction accumulation experiment process

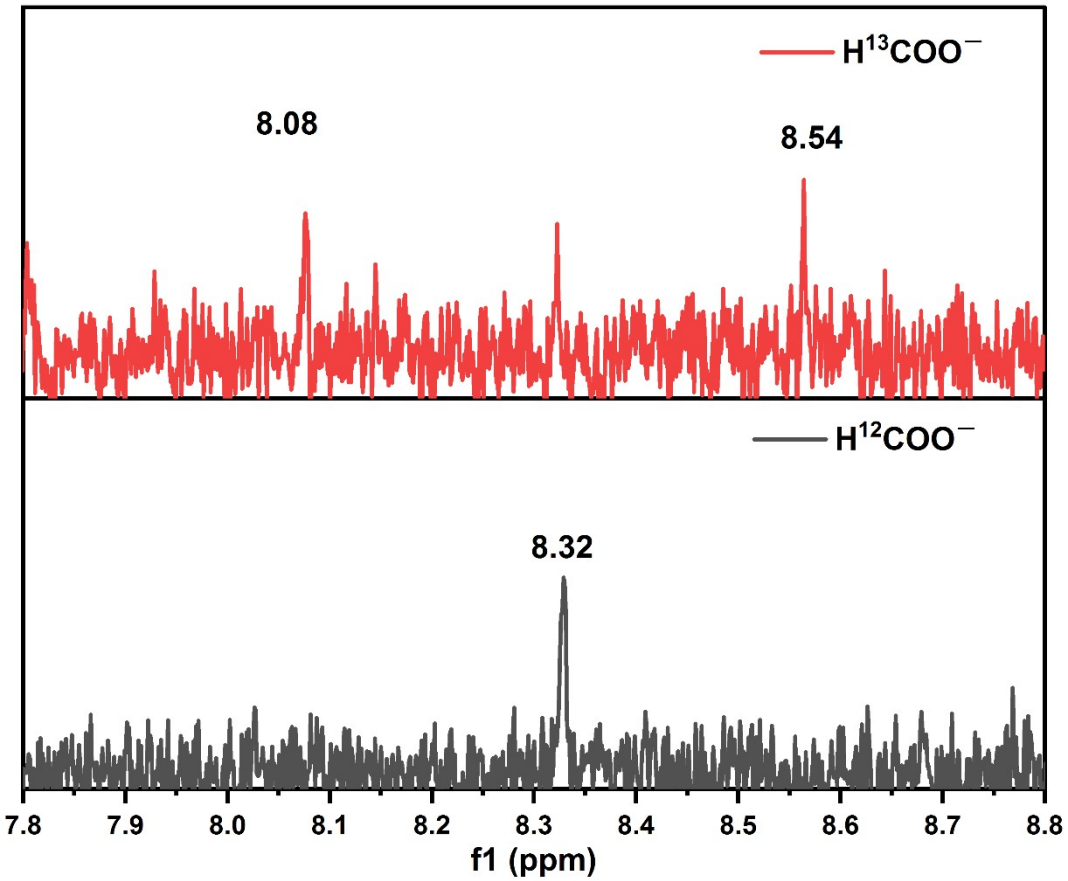

Figure S16. ^{1}H NMR spectra of the $H^{13}COO^{-}$ and $H^{12}COO^{-}$ generated in experiments

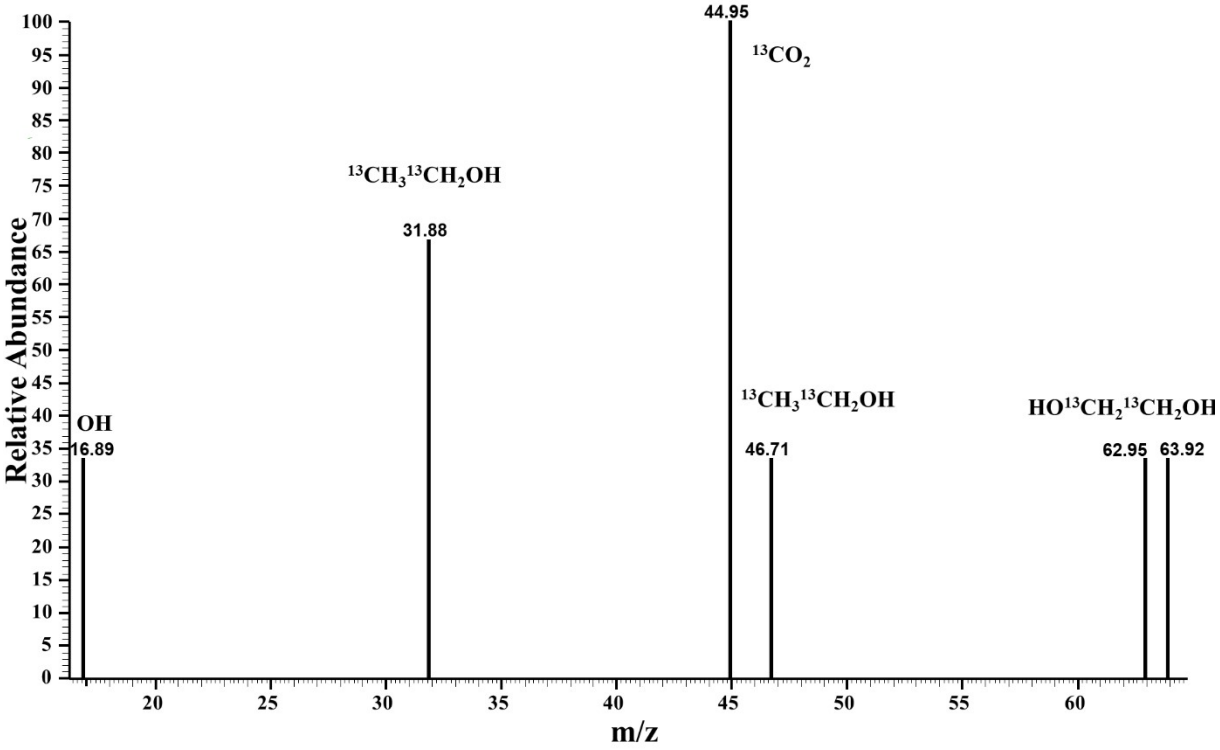

Figure S17. GC-MS analysis for products of $^{13}CO_2$ labeling experiment

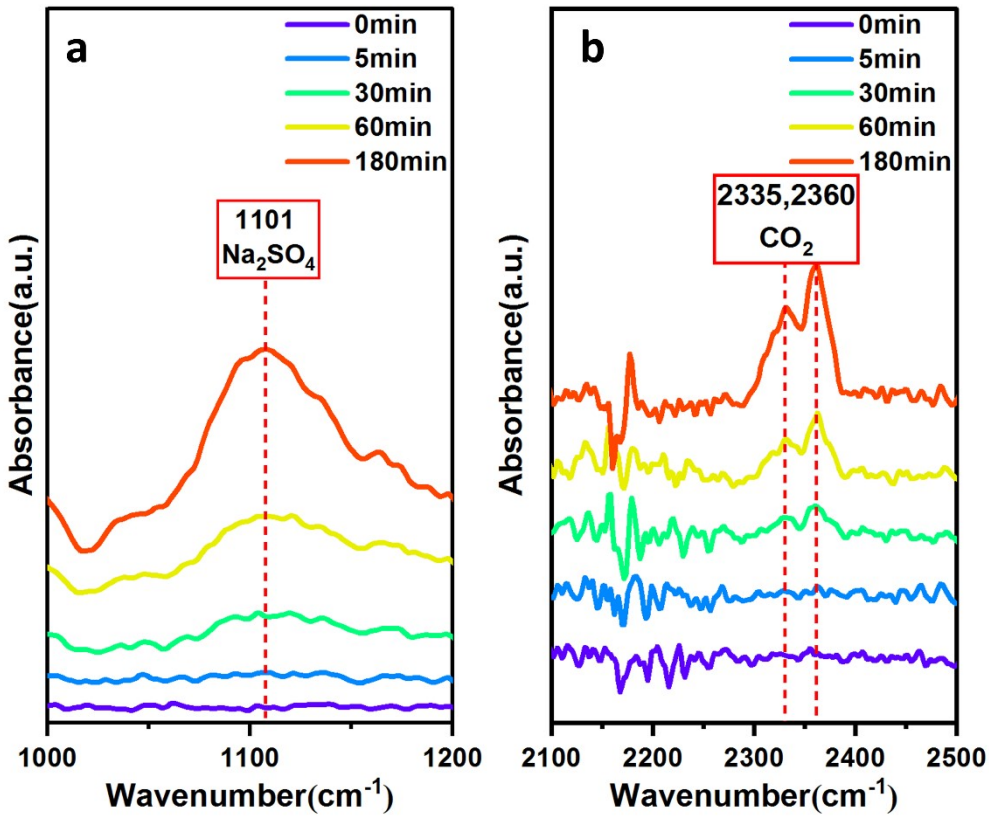

Figure S18. Operando FTIR spectra for the PEC CO_2 reduction process on the $NiMoO_4$/ZnO-3 in 0.1 M Na_2SO_3 H_2O electrolyte

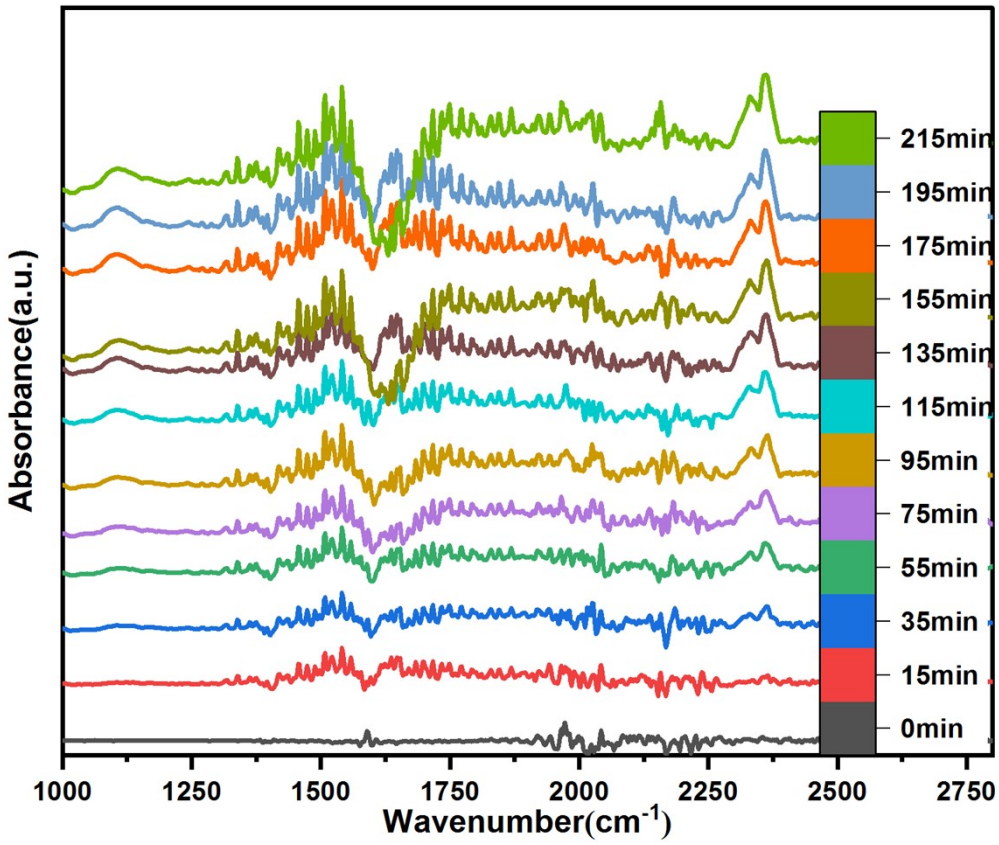

Figure S19. Operando FTIR spectra for the PEC CO_2 reduction process on the $NiMoO_4$/ZnO-3 in 0.1 M Na_2SO_3 H_2O electrolyte

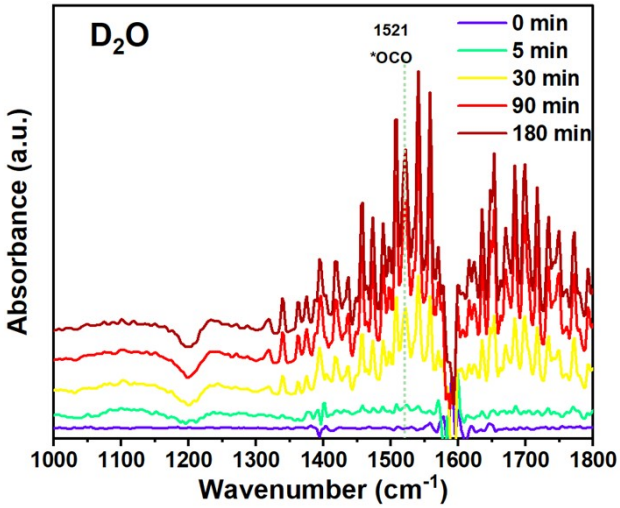

Figure S20. Operando FTIR spectra for the PEC CO_2 reduction process on the $NiMoO_4$/ZnO-3 in 0.1 M Na_2SO_3 D_2O electrolyte

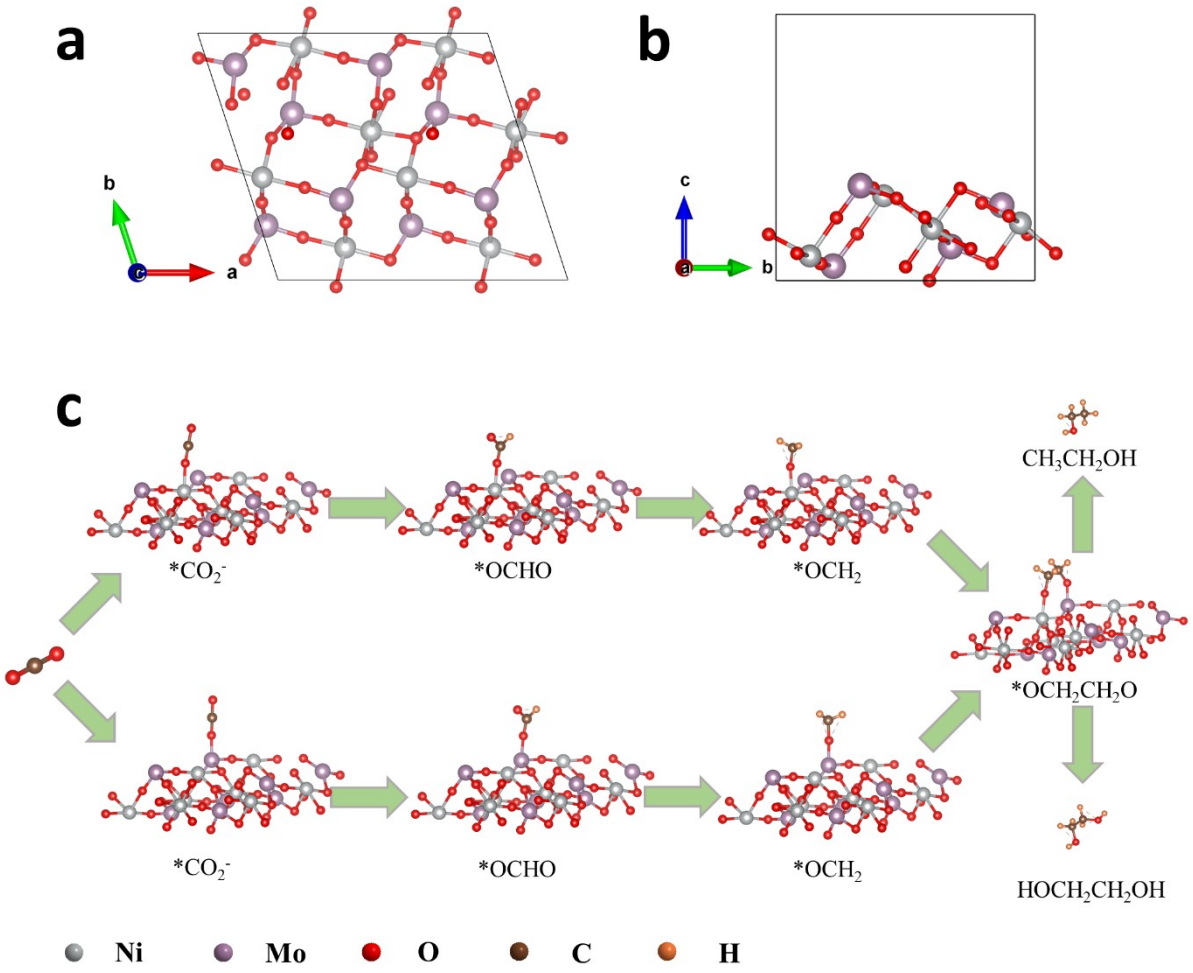

Figure 21. Structural model of $NiMoO_4$ used for the DFT calculations viewed along c-axis (a) and a-axis. (c)Views of DFT-calculated reaction pathways for the photoelectrochemical reduction of CO_2 to C2 products over Mo and Ni of $NiMoO_4$.

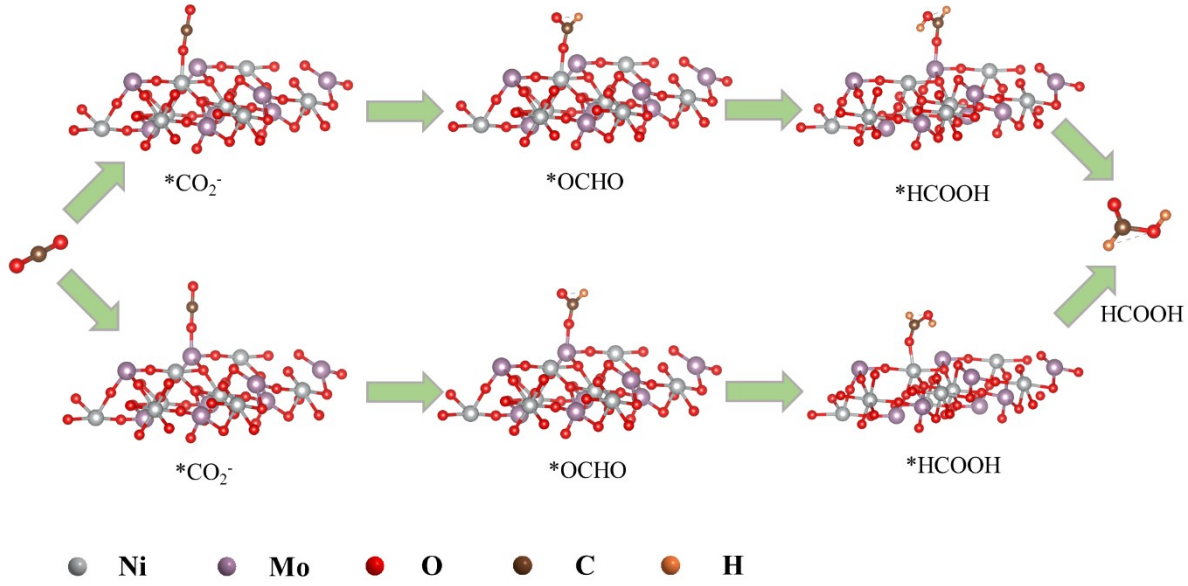

Figure 22. Views of DFT-calculated reaction pathways for the photoelectrochemical reduction of CO_2 to formic acid over Mo and Ni of $NiMoO_4$.

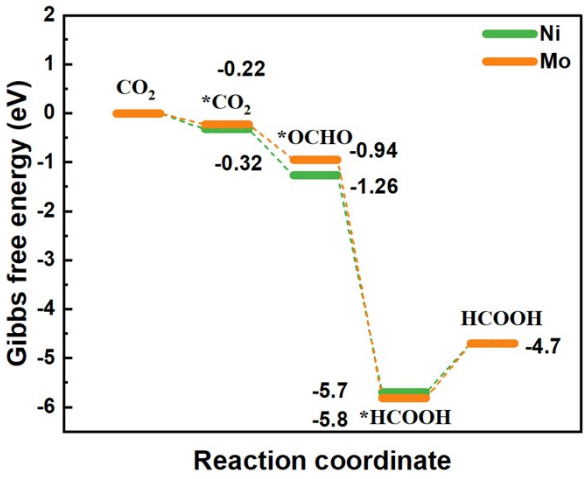

Figure 23. Gibbs free energy diagrams of the reduction of CO_2 into HCOOH with *OCHO mechanism on $NiMoO_4$

References

1. T. W. Kim and K. S. Choi, *Science*, 2014, **343**, 990-994.